Eur. Phys. J. B (2016) 89: 81
DOI: 10.1140/epjb/e2016-60986-8

THE EUROPEAN PHYSICAL JOURNAL B

Regular Article

Electronically-implemented coupled logistic maps*

Alexandre L'Her[1], Pablo Amil[1], Nicolás Rubido[1,2], Arturo C. Marti[1,a], and Cecilia Cabeza[1]

[1] Universidad de la República, Facultad de Ciencias, Iguá 4225, Montevideo, Uruguay
[2] University of Aberdeen, King's College, Institute for Complex Systems and Mathematical Biology, Aberdeen, AB24 3UE, UK

Received 30 December 2015 / Received in final form 4 February 2016
Published online 23 March 2016 –

Abstract. The logistic map is a paradigmatic dynamical system originally conceived to model the discrete-time demographic growth of a population, which shockingly, shows that discrete chaos can emerge from trivial low-dimensional non-linear dynamics. In this work, we design and characterize a simple, low-cost, easy-to-handle, electronic implementation of the logistic map. In particular, our implementation allows for straightforward circuit-modifications to behave as different one-dimensional discrete-time systems. Also, we design a coupling block in order to address the behavior of two coupled maps, although, our design is unrestricted to the discrete-time system implementation and it can be generalized to handle coupling between many dynamical systems, as in a complex system. Our findings show that the isolated and coupled maps' behavior has a remarkable agreement between the experiments and the simulations, even when fine-tuning the parameters with a resolution of $\sim 10^{-3}$. We support these conclusions by comparing the Lyapunov exponents, periodicity of the orbits, and phase portraits of the numerical and experimental data for a wide range of coupling strengths and map's parameters.

1 Introduction

Nowadays, there is a growing scientific interest in explaining the collective behaviors that emerge in complex systems [1–3], namely, systems composed of many non-linearly interacting subsystems. However, the analysis of complex systems is usually restricted to *toy-models* or numerical experiments [4–8], discarding the intractable parameter heterogeneities and random fluctuations (caused by intrinsic noise sources) found in real-world complex systems. Hence, the analysis of a synthetic complex system from a versatile experiment is always well-posed.

A well-known paradigmatic model that is used to understand chaotic behavior emerging from a trivial non-linear evolution is the logistic map [9–12]. It constitutes a tractable mathematical benchmark to characterize chaotic behavior (and other emerging phenomena) with a vast number of applications. Examples range from noise generators [13,14], encryption machines for secure communications [15–17] to models for ecology and demographic's research [7,9,12,18]. Even more, the logistic map has been extended to include more degrees of freedom [19–22]. Similarly, the inclusion of coupling between maps [23–25], for example, as in ecological models that address the effects of diversity or spatial heterogeneity in competing populations [7,8], shows promising results and increases the degrees of freedom. Analogously, a recent experimental study of coupled oscillators [26] shows the increase in complexity due to the coupled dynamics. Nevertheless, the interacting model of logistic maps still provides a solid benchmark to address emerging behaviors in other complex systems [6,12].

In this work, we design a versatile experimental implementation of a complex system composed of interacting logistic maps. Former attempts to electronically implement a logistic map are scarce and lack in simplicity [27–29], although manage to maintain control over all parameter range. Our logistic map design is simple and in a block form, has low-cost electronic components, it is easy-to-handle (allowing to maintain control over parameters), and also shows low power-consumption. Moreover, it allows to modify the map's block to include different behaviors, specifically, to become a different one-dimensional discrete-time system or even a continuous-time version of the system. The interaction between maps is designed as a coupling block that addresses the behavior of two coupled maps in the Kaneko style [24], however, this block is unrestricted to our case-study. In general, our coupling block can handle couplings between continuous-time dynamical systems and it also allows for straightforward extensions to many interacting dynamical systems. Such extensions make our model a versatile option to experimentally study different complex systems' behavior.

Our experimental findings show remarkable agreement with all numerical experiments, which we corroborate by exploring a wide range of parameters using high resolution

* Supplementary material in the form of three mp4 files available from the Journal web page at
http://dx.doi.org/10.1140/epjb/e2016-60986-8

[a] e-mail: marti@fisica.edu.uy

($\sim 10^{-3}$). Specifically, we explore variations in the logistic map's parameter and coupling strength for the uncoupled and coupled situations, respectively. Hence, we characterize the bifurcation cascades that the uncoupled and coupled systems exhibit [10] in both, numerical and experimental data, with high accuracy and signal-to-noise ratio. The comparative analysis between experiments and simulations shows that the level of performance and agreement is excellent. Moreover, we support this by analyzing the numerical and experimental data using Lyapunov exponents [11], orbit's periodicity [30], and phase portraits for the uncoupled and coupled cases.

The present work is organized as follows. We commence in Section 2 by introducing the model of coupled logistic maps and the methods used in the subsequent sections for the analysis of the experimental and numerical data. The experimental setup is presented in Section 3, starting with the electronic implementation of a single logistic map and the description of the coupling block and ending with the explanation on how to obtain an experimental discrete-time coupled system. The characterization of the dynamics of a single and a pair of maps is analyzed in Section 4 by means of bifurcations diagrams and stability charts displaying the periodicity (or chaoticity) as a function of the parameters. We end in Section 5 by summarizing our main conclusions.

2 Model and methods

2.1 Coupled logistic maps

The celebrated logistic map describes the discrete-time evolution of a closed population [9–12],

$$x_{n+1} = f(r, x_n) = r\, x_n\, (1 - x_n)\,, \tag{1}$$

where x_n represents the ratio of the population to a maximum value ($x_n \in [0, 1]$) at time n (discrete) and r is the control parameter, which is restricted to the interval $(0, 4]$ in order to keep the normalized population in the interval $[0, 1]$. The nonlinear term in the right hand side of equation (1) accounts for the population growth by reproduction (e.g., when the population size is small, $x_{n+1} \sim r\, x_n$) and for the starvation due to the limit imposed by the carrying capacity of the environment ($x_{n+1} \sim r[1 - x_n]$).

In this work, aside from the experimental implementation and characterization of the isolated logistic map (Eq. (1)), we analyze two coupled maps. Hence, for this case the state variables are $x_n^{(1)}$ and $x_n^{(2)}$, with control parameters r_1 and r_2, respectively. The evolution of these coupled maps is determined from

$$\begin{cases} x_{n+1}^{(1)} = (1-\epsilon)\, f\left(r_1, x_n^{(1)}\right) + \epsilon f\left(r_2, x_n^{(2)}\right), \\ x_{n+1}^{(2)} = (1-\epsilon)\, f\left(r_2, x_n^{(2)}\right) + \epsilon f\left(r_1, x_n^{(1)}\right), \end{cases} \tag{2}$$

where ϵ represents the coupling strength. This approach can be generalized to a network of N maps [24] by:

$$x_{n+1}^{(i)} = (1-\epsilon)\, f\left(r_i, x_n^{(i)}\right) + \epsilon \sum_{j=1}^{N} \frac{A_{ij}}{d_i} f\left(r_j, x_n^{(j)}\right), \tag{3}$$

where A_{ij} is the ij entry of the adjacency matrix of the network and $d_i = \sum_j A_{ij}$ is the ith node degree.

2.2 Dynamical behavior characterization

Lyapunov exponents provide a useful characterization of a dynamical system in terms of how sensible the system is to small changes in its initial conditions [11]. Specifically, they quantify the average divergence of an infinitesimal displacement from an unperturbed reference orbit and are related to the factor by which the infinitesimal displacement grows or shrinks. For a generic dynamical system, the number of Lyapunov exponents is equal to the dimension of the system, i.e., the number of independent perturbations. In many applications it is sufficient to calculate only the largest Lyapunov exponent, $\lambda_{\max}$, since in general, $\lambda_{\max} > 0$ ($\lambda_{\max} < 0$) implies the presence of chaotic (periodic) behavior.

In the case of an isolated logistic map, namely, a one-dimensional discrete-time dynamical system, there is a single Lyapunov exponent, λ, to determine. This exponent is directly obtained from [11]

$$\lambda(r) = \lim_{N\to\infty} \frac{1}{N} \sum_{n=1}^{N-1} \ln\left[r\ (1 - 2\, x_n)\right], \tag{4}$$

where r is the map's parameter (Eq. (1)) and x_n for $n = 1$ corresponds to the initial condition of the map. For finite-size orbits, namely, when the limit is absent, λ is a finite-time Lyapunov exponent (FLE), which we name in what follows as Lyapunov exponent. However, for sufficiently long time-series ($N \gg 1$), the FLE converges asymptotically to the value of (Eq. (4)).

Another useful characterization for the coupled maps behavior is done by quantifying the periodicity of their orbits [30]. In other words, looking at the periodic properties of the resultant orbits for every dynamical regime. Specifically, we measure the periodicity of an orbit as a function of the parameters for the coupled system. In order to measure this periodicity, we define the period of the coupled system by building a data sequence that is defined by concatenating the state variables at consecutive times. For example, in our case-study, the coupled maps orbit results in a concatenated time-series as

$$\ldots x_n^{(1)}, x_n^{(2)}, x_{n+1}^{(1)}, x_{n+1}^{(2)}, \ldots \tag{5}$$

Consequently, the period of the system is identified by the periodicity of the compound state sequence divided by the number of units, which in this work is 2.

3 Electronic implementation

Our logistic map design is divided into two main parts. A logistic-map block (LMB), which makes an analog logistic function (as in the right-hand side of Eq. (1)), and a sample-and-hold block (SHB), which samples the voltage

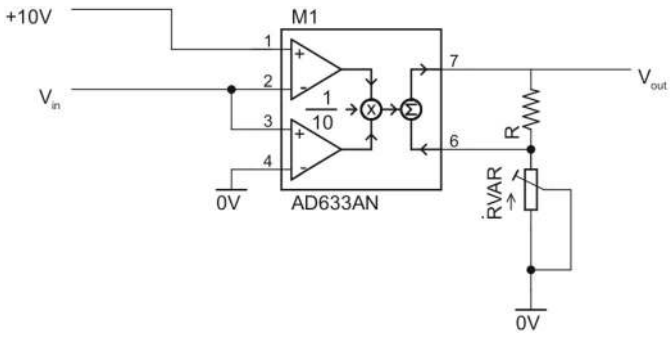

Fig. 1. Diagram of the electronic circuit that reproduces the logistic function. Namely, the output voltage is a quadratic function of the input voltage.

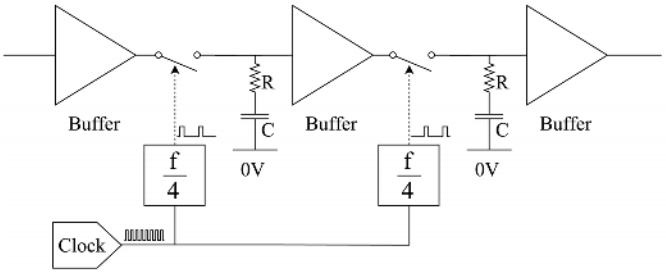

Fig. 2. Schematic diagram of the sample-and-hold block. This block is implemented to produce a step-wise evolution of the electronic circuit, hence, a discrete-time evolution is achieved.

of the continuously varying analog-signal of the LMB and holds its value at a constant level for a specified period of time. Hence, the output is an analog time-series that varies its values step-wise, modeling the discrete evolution of a map. This electronic implementation provides great flexibility since it allows to design other maps by modifying the LMB or to implement time-delayed models (as in Refs. [31,32]) by modifying the SHB. Furthermore, this design is chosen for scalability, meaning that its implementation allows for the direct introduction of coupling between several individual units and with arbitrary connections among them. In other words, our implementation in blocks allows to set different networks of coupled maps without the commonly found limitation of an increasing complexity in the electronic setup. In particular, the coupling between two logistic maps as in equation (2) is designed in a similar block form, which we name the coupling block (CB). Hence, we retain the scalability of the system allowing for a possible extension of the design to contemplate a coupled N-maps dynamic (Eq. (3)).

3.1 The logistic-map block

The LMB is designed to reproduce the logistic function of the right-hand side of equation (1) and is shown in Figure 1. The present implementation uses an analog multiplier AD633, whose input range is ±10 V and output range ±11 V. The output voltage, V_{out}, is obtained using the information provided by the manufacturer, namely,

$$V_{out}(t) = \frac{[V_1(t) - V_2(t)]\,[V_3(t) - V_4(t)]}{V_s} + V_6(t), \qquad (6)$$

$V_i(t)$ $(i = 1, \ldots, 6)$ being the voltage at the terminals indicated in Figure 1 and $V_s = 10$ V being the saturation voltage of the AD633. For this circuit, assuming ideal behavior of the components and applying Kirchhoff's laws [27], we find from equation (6) that

$$V_{out}(t) = \left(1 + \frac{R_{var}}{R}\right) \frac{V_{in}(t)\,(V_s - V_{in}(t))}{V_s}, \qquad (7)$$

where $R = 1$ kΩ and R_{var} can be set between 0 Ω and 3 kΩ. The different values of R_{var} are obtained using a step-by-step motor attached to a multi-turn potentiometer and controlled by a National Instrument Data Acquisition (NIDAQ).

The voltages of the electronic circuitry are identified with the state-variables of equation (1) by $x_n \mapsto V_{in}/V_s$ and $x_{n+1} \mapsto V_{out}/V_s$, and the control parameter with

$$r \equiv \left(1 + \frac{R_{var}}{R}\right). \qquad (8)$$

Our analysis of the LMB takes into account solely the variation of r in the interval $(1, 4)$. The reason is that, since $R = 1$ kΩ under our implementation, the interval $r \in (0, 1)$ where the dynamics of the map corresponds to a stable fixed-point is unreachable. Also note that, when $r \simeq 4$, the electronic noise can take the voltage to values higher than V_s, hence, saturating the analog multiplier. Consequently, in the analysis to characterize the system we set $r < 4$ such that we always avoid this problem.

3.2 The sample-and-hold block

In Figure 2 we schematically show the SHB based on two LF398 circuits (the two left-most buffers) and an op-amp circuit (the right-most buffer) [28]. It samples the voltage from the input terminal at an instant of time, keeps its value in the hold capacitor, and then releases its value from the output terminal one clock-period later. Every two clock periods, the roles of both LF398 are interchanged. This switching results in a discontinuous evolution of the whole circuit (LMB plus SHB), where at each instant of time a value of x_n is obtained.

The optimal clock's frequency, which sets the time lapse between consecutive values of the output voltage, must be chosen taking into account several experimental constrains. On the one hand, there is a limit given by the time it takes for the SHB to charge the capacitors. On the other hand, the existence of parasitic capacitance, bias currents in the operational amplifiers or other components, and leakage currents in the capacitors, also sets limits to the clock's frequency. Moreover, the response time for the rest of the circuit to stabilize after any change, i.e., the time needed by the LMB and the coupling to stabilize the output, constitutes an upper bound for the clock's frequency. However, from a practical point of view, the

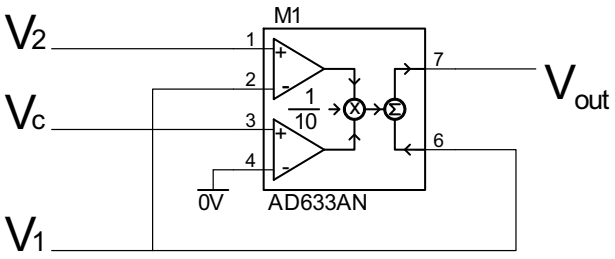

Fig. 3. Diagram of the coupling circuit. The output voltage from this circuit linearly relates both input voltages, V_1 and V_2, with a coupling intensity given by V_c.

clock's frequency should be as high as possible to reduce the time necessary to perform the experiments and obtain long time-series. Consequently, we have chosen the clock's frequency to be in the range between 10 kHz to 20 kHz.

3.3 The coupling block

The experimental setup for the coupling circuit is depicted in Figure 3. In order to couple two logistic maps, we require a coupling circuit for each map. Moreover, to retain the possibility of extending our design to implement networks of maps, we design a coupling block (CB) as in Figure 4. Hence, the LMB is connected to the SHB to define the discrete-time evolution of the system and it is also connected to the CB to implement the coupled evolution according to equation (2). Specifically, after taking into account the AD633 in Figure 3, we obtain V_{out} as:

$$V_{out}(t) = \left(1 - \frac{V_c}{V_s}\right) V_1(t) + \frac{V_c}{V_s} V_2(t), \qquad (9)$$

where V_c is the control voltage for our CB, namely, the coupling strength between the maps; $\epsilon \equiv V_c/V_s$. In particular, when V_c changes between 0 and V_s (the saturation voltage), ϵ changes between 0 and 1. Thus,

$$x_{out}(t) = \frac{V_{out}(t)}{V_s} = (1-\epsilon)\, x_1(t) + \epsilon\, x_2(t), \qquad (10)$$

where we have identified the voltages $V_1(t)$ and $V_2(t)$ with the corresponding logistic states $x^{(1)}(t) = V_1(t)/V_s$ and $x^{(2)}(t) = V_2(t)/V_s$, respectively.

In order to have high accuracy and control over the changes in V_c we use the analog output of the NIDAQ, which allows to set V_c with a precision of ± 20 mV (according to the data-sheet). This precision is even lower than the 30 mV noise level we observe experimentally in our time-series data. Moreover, we tested the excellent performance of the CB by critically comparing the experimental time-series with numerically generated time-series of equation (2).

3.4 Electronic map

The discrete time-evolution of the experimental system is obtained after processing the continuous step-wise evolution of the LMB plus SHB output. The conversion from

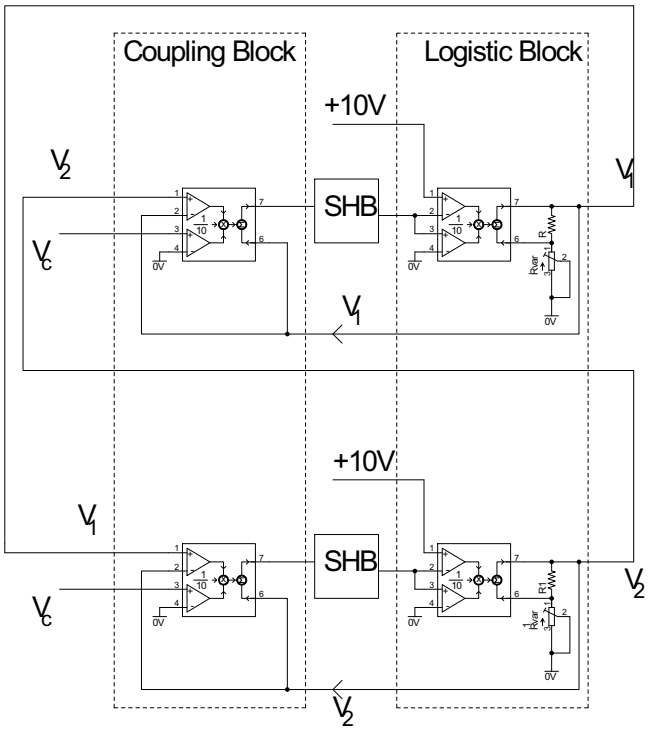

Fig. 4. Block diagram of two coupled logistic maps. SHB stands for the sample-and-hold block of Figure 2.

the combined circuit's output signal to the discrete-time state variable of the logistic map, namely, x_n, consists in taking the mean value for each plateau. Specifically, x_n is found by the hold value of the sampling of the LMB voltage every four clock-periods. A working example of this process is shown in Figure 5, where the continuous signal registered from the LMB plus SHB is represented by the dashed line and the corresponding discrete evolution is represented by the signaled square points. As a result, the storage space that is needed to save the output signal is reduced and we obtain a discrete-time evolution of the system, i.e., the logistic map's evolution.

In particular, our findings show that there is a remarkable agreement between the experimental values of r, which are found from equation (8), and the r we found from fitting this time-series output to a quadratic function. For example, the output of the LMB using an experimental control parameter of $r = 3.5 \pm 0.1$ (Eq. (8)), results in a time-series with a fitted value of $r = 3.5005$ and regression coefficient of 0.9999.

4 Results and analysis

4.1 Isolated logistic map

To corroborate that our electronic model reproduces correctly the logistic map's behavior, the experimental results are compared with the numerical simulations of equation (1). All comparisons are performed by neglecting a transient of 10^4 iterations, which eliminates the orbit's dependency on the initial condition.

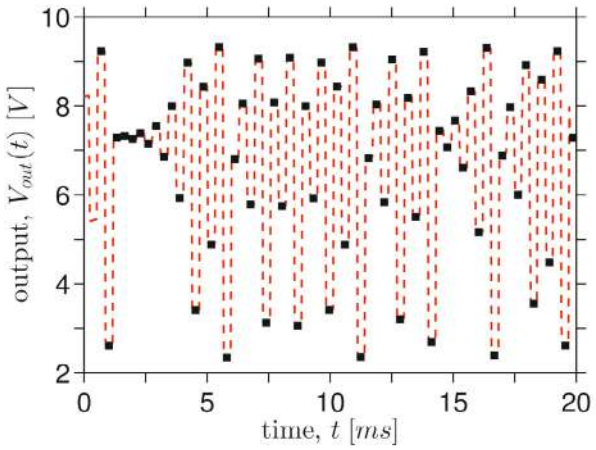

Fig. 5. Experimental output voltage obtained from our logistic-map block (LMB) implementation with its sample-and-hold block (SHB). The analog output signal is represented by the dashed line and the discrete map evolution that is obtained from this output is represented by the filled squares. The data corresponds to a single LMB plus SHB for the case where there is coupling between two of these circuits with a strength $\epsilon = 0.5$ and the circuit's parameters are in the chaotic regime ($r = 3.8$).

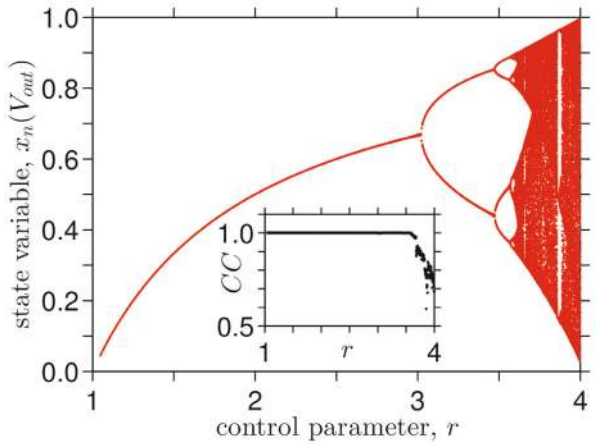

Fig. 6. Bifurcation diagram for the output voltages of our logistic map's electronic implementation. The diagram is constructed discarding 10^4 initial time-iterations and taking the next 256 values of the discrete-time voltages (x_n) as a function of 1024 different control parameter (r) values. It shows the distinctive traces of the logistic map's route to chaos. The correlation function ($CC(x, y) = \langle xy \rangle / \sigma_x \sigma_y$) between the experimental data and the numerical simulation for each r are shown in the inset, where small (<30%) deviations are found for parameter values close to the chaotic region ($r > 3.5$).

The experimental bifurcation diagram as a function of the control parameter is shown in Figure 6. As it is seen, it reproduces the essential characteristics of the logistic map's Feigenbaum diagram [10,11]. The agreement is quantified by the high value that the correlation function, CC, between the experimental and the simulated signal have, which is shown in the inset of Figure 6, specially for the periodic regions. In particular, the slight departures of CC from unity for $r > 3.5$ are a consequence of chaos and small shifts in the experimental control parameter value. However, as it is seen from the figure, these shifts leave the diagram virtually unaffected with respect to the Feigenbaum diagram of the logistic map [10,11].

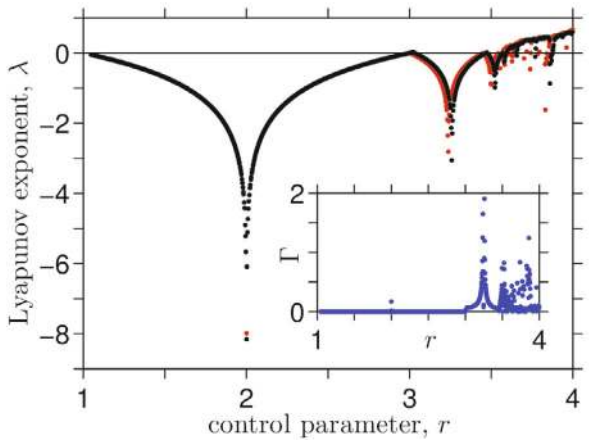

Fig. 7. Experimentally (black online) and numerically (red online) obtained Lyapunov exponents (λ) for a logistic map. Both exponents are found from 10^4 iterations for 1024 different control parameter (r) values. The differences between these exponents for each value of r are quantified in the inset by the error function, $\Gamma \equiv |\lambda_{sim} - \lambda_{exp}|$, where $\lambda_{exp}(\lambda_{sim})$ is the experimental (numerical) Lyapunov exponent for the particular time-series.

In order to further analyze the dynamical behavior of our electronically implemented map, we compare the Lyapunov exponents of the experimentally and numerically obtained time-series. In particular, the experimental Lyapunov exponents are calculated from $N = 10^4$ data points, instead of the $N = 256$ data points that are used to construct the experimental diagram of Figure 6. Similarly, the numerical simulations are iterated $N = 10^4$ times. The resultant Lyapunov exponents for both cases are shown in Figure 7. The Pearson's correlation coefficient between the experimental and the simulated Lyapunov exponents we find is $R = 0.9816$. Moreover, we calculate the error between the exponents, $\Gamma \equiv |\lambda_{exp} - \lambda_{sim}|$, for each parameter r value, which is shown in the inset of Figure 7. Γ shows, as the bifurcation diagram does, that there is a remarkable agreement between the experimental and the numerical data in the regions displaying periodic behavior. The discrepancies that are found in the chaotic region correspond to a small shift in the experimental control parameter, r, which looks as a rigid body translation of the experimental system with respect to the simulation. Nevertheless, these analysis reveals that our electronic implementation reproduces the behavior of the logistic map with high accuracy, specially for $r < 3$.

4.2 Two coupled maps

Here we present the experimental and numerical results for the coupled dynamics of two logistic-maps.

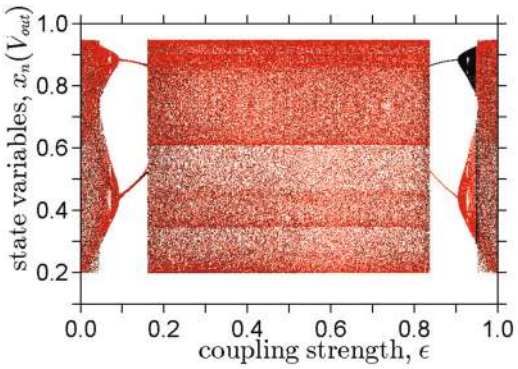

(a)

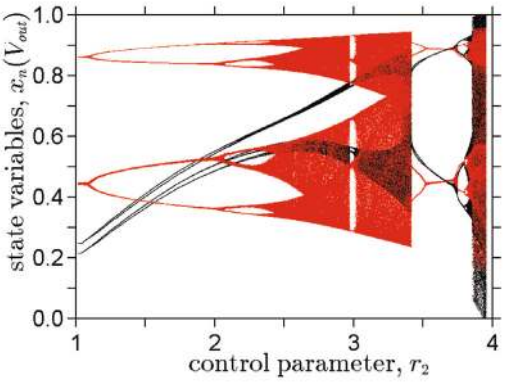

(b)

Fig. 8. Experimental bifurcation diagrams. Panel (a) is obtained from increasing the coupling strength between two identical maps, where both logistic maps are in the chaotic region ($r = 3.8$) and the increments in ϵ are set to 0.01. Panel (b) is obtained by decreasing the heterogeneity between the maps, namely, $r_1 = 3.8$, $\epsilon = 0.1$, and we increase r_2. The light (red online) and dark (black online) dots on both panels correspond to the time-series from the maps $x_n^{(1)}$ and $x_n^{(2)}$, respectively.

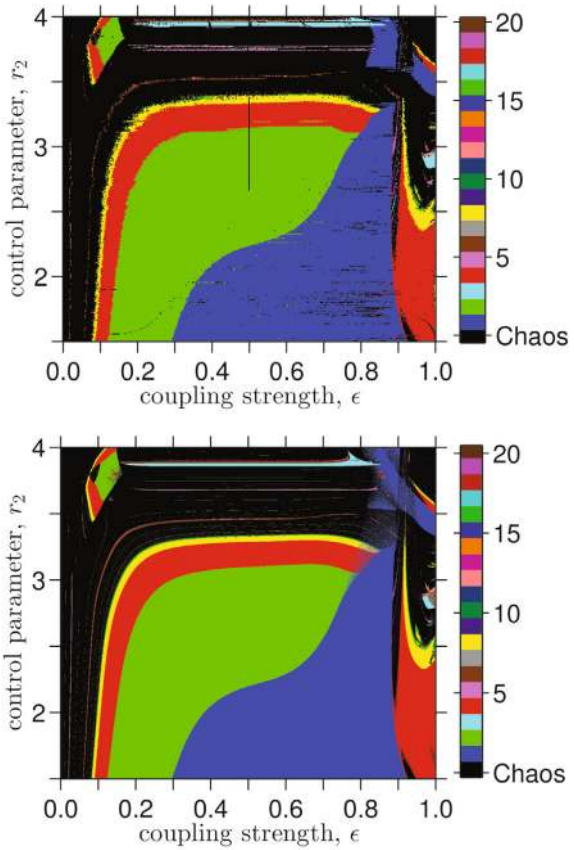

Fig. 9. Orbit's periodicity for the parameter space of two coupled logistic-maps. The top (bottom) panel shows the experimental (numerical) periodicity of the orbits in color scale. The parameter space is constructed by fixing $r_1 = 3.8$ and changing, r_2, and the coupling strength, ϵ. Experimental (numerical) resolution: 512×512 (2048×2048) parameter points.

The bifurcation diagrams for identical maps as a function of the coupling strength, ϵ, are displayed in Figure 8a, where the map's parameters are set equally to $r_1 = r_2 = r = 3.8$. Due to the presence of coupling between the maps, namely, $\epsilon > 0$, the resultant dynamics shows both chaotic (regions where points spread vertically in Fig. 8a) and periodic (thin lines of points in Fig. 8a that stay narrow over a range of ϵ values) behavior. These behaviors contrast the exclusively chaotic behavior that the maps show for this parameter value ($r = 3.8$) in the absence of coupling, as it is seen on the left of Figure 8a for $\epsilon = 0$. Two videos for the bifurcation development are presented on the Supplementary Material* (SM) corresponding to the weak (Fig. 8a left) and strong (Fig. 8a right) coupling scenarios. These videos show the phase space portraits as coupling ϵ is increased from 0 to 0.12 (0.82 to 1), hence, changing the chaotic (periodic) behavior and shifting it to a periodic (chaotic) state. Also, the videos show how quasi-periodic behavior emerges before periodic or chaotic behavior does.

A non-symmetrical situation is depicted in the bifurcation diagram of Figure 8b. We are fixing one map's parameter ($r_1 = 3.8$) and the coupling strength ($\epsilon = 0.1$) but we are changing the other map's parameter (r_2). Hence, this diagram is the quantification of how the decrease in heterogeneity between the maps (namely, the increase of r_2 from 1.0 to 3.8) causes bifurcations to emerge [23–25]. Hence, we shift from the periodic region (left side of Fig. 8b) to the chaotic region (right side of Fig. 8b). However, although $r_2 = 1$ in the periodic region, corresponding to a fixed-point state, due to the weak coupling between the maps ($\epsilon = 0.1$) it shows a period-2 behavior. This is also supported by a phase space portrait video we are presenting in the SM.

In order to continue the quantitative comparison between the experimentally implemented maps and the numerical simulations, we show in Figure 9 the periods that the orbits have as a function of the coupling strength (ϵ, horizontal axes) and the map's control parameter (r_2, vertical axes), namely, the map's heterogeneity. Specifically, we fix $r_1 = 3.8$ and vary ϵ and r_2. These results, experimental (Fig. 9a) and numerical (Fig. 9b), show a remarkable concordance, even though we are using an

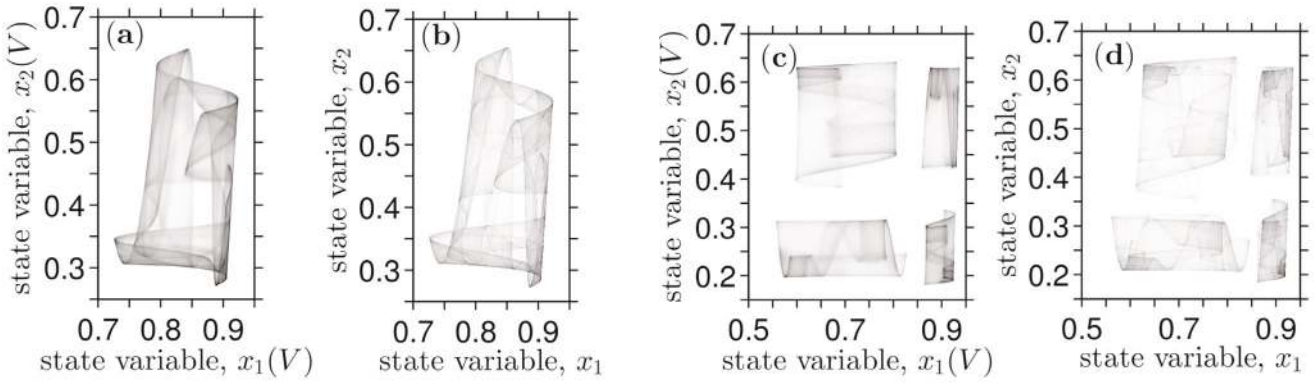

Fig. 10. Phase space comparison between coupled logistic maps. Panels (a) and (b) show the attractors that are found by fixing $r_1 = 3.22$, $r_2 = 3.79$, and $\epsilon = 0.937$, on the experimental and on the numerical coupled system, respectively. Similarly, panels (c) and (d) show the experimental and numerical attractor for $r_1 = 2.60$, $r_2 = 3.79$, and $\epsilon = 0.963$. The experimental time-series length to construct these portraits is of $\sim 50 \times 10^6$, with an even larger numerical time-series length.

outstanding resolution for both axis (10^{-3}). We highlight the richness of the several coexisting motions in Figure 9 that are obtained from this method. The different dynamical behaviors are revealed explicitly in these diagrams, in contrast with the unresolved cases when using other indicators, as the Lyapunov exponents.

As a qualitative comparison, we show in Figure 10 two phase-space portraits for the strongly coupled system ($\epsilon \sim 1$) on two particular scenarios. The resulting attractors show remarkable complexity, nevertheless, the experimental (Figs. 10a and 10c) and numerical (Figs. 10b and 10d) attractors still remain remarkably close. This conclusion holds for a wide range of parameters and other phase-space portraits, which we are omitted here.

5 Conclusion

In this paper, we showed that our simple implementation represents correctly the behavior of the logistic map, and brings more possibilities for the study of chaos dynamics than previous implementations. We also implemented a Kaneko coupling, which we use to show that our logistic-map design allows us to couple several maps. In particular, we made a thorough analysis of the coupled dynamics of two logistic-maps by critically comparing numerical and experimental data using Lyapunov exponents, orbit's periodicity, and phase-space portraits. Instead of logistic maps, different functions could be equally implemented using our approach.

We can easily expand the system by adding extra couplings and maps since the coupling between two maps performed faultlessly. In particular, when studying the dynamics of two coupled maps, we observed that chaotic synchronization was possible in a wide range of coupling strengths, thus showing the robustness of the synchronous behavior and opening the question of how will a large set of coupled oscillators behave in an experimental system. The increase in size of our electronic design by the inclusion of more maps would allow us to make a full working network and study its behaviors, which are widely studied theoretically and numerically but generally lack experimental study. In a field dominated by numerical simulations, our electronic design allows us to have a flexible system for future studies. Also, the implementation of a working network of many interacting chaotic oscillators could result in a system (if well calibrated) presenting high-dimensional chaotic dynamics, useful in a wide variety of applications [6].

We acknowledge financial support from Programa de Desarrollo de las Ciencias Básicas (PEDECIBA), Uruguay.

References

1. A.L. Barabasi, *Linked: How Everything is Connected to Everything else and what it Means* (Plume Editors, 2002)
2. S.H. Storgatz, *Sync: the Emerging Science of Spontaneous Order* (Hyperion, 2003)
3. A. Barrat, M. Barthelemy, A. Vespignani, *Dynamical Processes on Complex Networks* (Cambridge University Press, 2008)
4. E.N. Lorenz, J. Atmospheric Sci. **20**, 130 (1963)
5. A.T. Winfree, in *The Geometry of Biological Time* (Springer Science and Business Media, 2001), Vol. 12
6. K. Kaneko, Chaos **25**, 097608 (2015)
7. A.L. Lloyd, J. Theor. Biol. **173**, 217 (1995)
8. B.E. Kendall, G.A. Fox, Theor. Pop. Biol. **54**, 11 (1998)
9. R.M. May et al., Nature **261**, 459 (1976)
10. M.J. Feigenbaum, J. Stat. Phys. **19**, 25 (1978)
11. K.T. Alligood, T.D. Sauer, J.A. Yorke, *Chaos: An Introduction to Dynamical Systems* (Springer, 1996)
12. P. Collet, J.P. Eckmann, *Iterated Maps on the Interval as Dynamical Systems* (Springer Science & Business Media, 2009)
13. G. McGonigal, M. Elmasry, Circuits Syst. IEEE Trans. **34**, 981 (1987)
14. S.C. Phatak, S.S. Rao, Phys. Rev. E **51**, 3670 (1995)
15. N.K. Pareek, V. Patidar, K.K. Sud, Image Vision Comput. **24**, 926 (2006)

16. N. Singh, A. Sinha, Opt. Lasers Eng. **48**, 398 (2010)
17. S.E. Borujeni, M.S. Ehsani, Appl. Math. **6**, 773 (2015)
18. L. Stone, Nature **365**, 617 (1993)
19. M.S. Baptista, I. Caldas, Chaos Solitons Fractals **7**, 325 (1996)
20. M.S. Baptista, I. Caldas, Int. J. Bifurc. Chaos **7**, 447 (1997)
21. E. Campos-Cantón, R. Femat, A. Pisarchik, Commun. Nonlinear Sci. Numer. Simul. **16**, 3457 (2011)
22. A.G. Radwan, J. Adv. Res. **4**, 163 (2013)
23. K. Kaneko, Prog. Theor. Phys. **69**, 1427 (1983)
24. K. Kaneko, Physica D **41**, 137 (1990)
25. Y.L. Maistrenko, V.L. Maistrenko, A. Popovich, E. Mosekilde, Phys. Rev. E **57**, 2713 (1998)
26. L.Q. English, Z. Zeng, D. Mertens, Phys. Rev. E **92**, 052912 (2015)
27. P. Horowitz, W. Hill, *The Art of Electronics* (Cambridge University Press, 1989)
28. M. Suneel, Sadhana **31**, 69 (2006)
29. M. García-Martínez, I. Campos-Cantón, E. Campos-Cantón, S. Čelikovskỳ, Nonlin. Dyn. **74**, 819 (2013)
30. S.T. Welstead, T.L. Cromer, Comput. Graphics **13**, 539 (1989)
31. P. Amil, C. Cabeza, C. Masoller, A.C. Martí, Circuits and Systems II: Express Briefs, IEEE Trans. **62**, 681 (2015)
32. P. Amil, C. Cabeza, C. Masoller, A.C. Martí, Chaos **25**, 043112 (2015)